

# Thermal Imaging with Novel Infrared Focal Plane Arrays and Quantitative Analysis of Thermal Imagery

S. D. Gunapala, S. B. Rafol, S. V. Bandara, J. K. Liu, J. M. Mumolo, A. Soibel, and D. Z. Ting

Center for Infrared Sensors, Jet Propulsion Laboratory, California Institute of Technology, Pasadena, CA 91109, U.S.A.

## ABSTRACT

We have developed a single long-wavelength infrared (LWIR) quantum well infrared photodetector (QWIP) camera for thermography. This camera has been used to measure the temperature profile of patients. A pixel co-registered simultaneously reading mid-wavelength infrared (MWIR)/LWIR dual-band QWIP camera was developed to improve the accuracy of temperature measurements especially with objects with unknown emissivity. Even the dual-band measurement can provide inaccurate results due to the fact that emissivity is a function of wavelength. Thus we have been developing a four-band QWIP camera for accurate temperature measurement of remote object.

**Key Words:** Quantum-wells, Focal planes, Dual-band infrared, Thermography

## 1. INTRODUCTION

There are many applications that require long wavelength, large, uniform, reproducible, low cost, low  $1/f$  noise, low power dissipation, and radiation hard infrared (IR) focal plane arrays (FPAs). However, the need for smaller, lighter and lower cost imaging radiometers is now apparent, particularly in missions that combine different types of remote sensing instruments. A quantum well designed to detect infrared (IR) light is called a quantum well infrared photodetector (QWIP). An elegant candidate for QWIP is the square quantum well of basic quantum mechanics [1]. When the quantum well is sufficiently deep and narrow, its energy states are quantized (discrete). The potential depth and width of the well can be adjusted so that it holds only two energy states: a ground state near the well bottom, and a first excited state near the well top. A photon striking the well will excite an electron in the ground state to the first excited state, then an externally-applied voltage sweeps it out producing a photocurrent (Fig. 1). Only photons having energies corresponding to the energy separation between the two states are absorbed, resulting in a detector with a sharp absorption spectrum. Designing a quantum well to detect light of a particular wavelength becomes a simple matter of tailoring the potential depth and width of the well to produce two states separated by the desired photon energy. The GaAs/ $\text{Al}_x\text{Ga}_{1-x}\text{As}/\text{In}_y\text{Ga}_{1-y}\text{As}$  material system allows the quantum well shape to be tweaked over a range wide enough to enable light detection at wavelengths longer than  $\sim 3 \mu\text{m}$ . Fabricated entirely from large bandgap materials which are easy to grow and process, it is now possible to obtain large uniform FPAs of QWIPs tuned to detect light at wavelengths from 3 to  $25 \mu\text{m}$  in the GaAs/ $\text{Al}_x\text{Ga}_{1-x}\text{As}/\text{In}_y\text{Ga}_{1-y}\text{As}$  material system [2-5].

Improving QWIP performance depends largely on minimizing the parasitic current that plagues all light detectors, the dark current (the current that flows through a biased detector in the dark, i.e., with no photons impinging on it). As we have discussed elsewhere [5], at temperatures above 45 K, the dark current of the long-wavelength infrared (LWIR) QWIP is entirely dominated by classic thermionic emission of ground state electrons directly out of the well into the energy continuum. Minimizing this last component is critical to the success of the QWIP as it allows highly-desirable high-temperature camera operation.

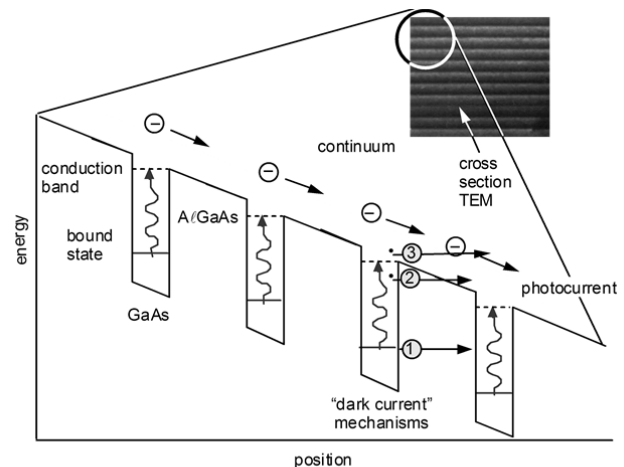


**Fig. 1:** Schematic diagram of the conduction band in a bound-to-quasibound QWIP in an externally applied electric field. Absorption of IR photons can photoexcite electrons from the ground state of the quantum well into the continuum, causing a photocurrent. Three dark current mechanisms are also shown: ground state tunneling (1); thermally assisted tunneling (2); and thermionic emission (3). The inset shows a cross-section transmission electron micrograph of a QWIP sample.

Therefore, we have designed the *bound-to-quasibound* [1] quantum well by placing the first excited state exactly at the well top as shown in Fig. 1. Dropping the first excited state to the well top causes the barrier to thermionic emission (roughly the energy height from the ground state to the well top) to be  $\sim 10$  meV more in our bound-to-quasibound QWIP than in the bound-to-continuum QWIP, theoretically causing the dark current to drop by a factor of  $\sim 6$  at a temperature of 70 K [2,3]. The dark current as a function of temperature of the  $8.5 \mu\text{m}$  peaked bound-to-quasibound QWIP is shown in Fig. 2. This compares well with the factor of  $\sim 4$  drop we experimentally observe compared to the bound-to-continuum QWIP having the same peak wavelength.

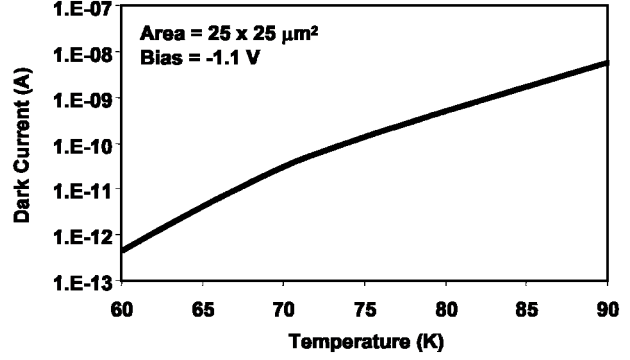


**Fig. 2:** Dark current of  $8.5 \mu\text{m}$  peaked bound-to-quasibound QWIP as a function of temperature. Data were taken with a  $200 \mu\text{m}$  diameter test structure and normalized to  $25 \times 25 \mu\text{m}^2$  pixel.

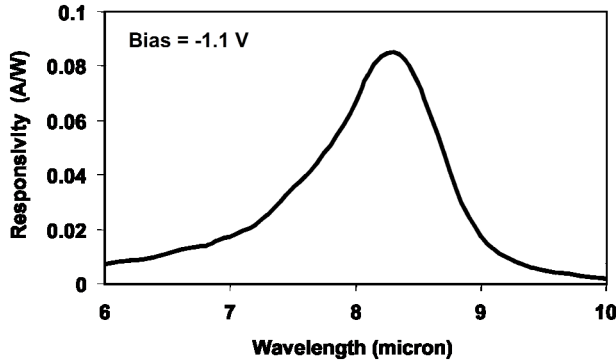


**Fig. 3:** Responsivity spectrum of a bound-to-quasibound LWIR QWIP test structure at temperature  $T = 77 \text{ K}$ . The spectral response peak is at  $8.5 \mu\text{m}$  and the long wavelength cutoff is at  $8.9 \mu\text{m}$ .

## 2. TEST STRUCTURE RESULTS

Each period of the multi-quantum well (MQW) structure consists of a  $45 \text{ \AA}$  well of GaAs (doped  $n = 5 \times 10^{17} \text{ cm}^{-3}$ ) and a  $500 \text{ \AA}$  barrier of  $\text{Al}_{0.3}\text{Ga}_{0.7}\text{As}$ . Stacking many identical quantum wells (typically 50) together increases photon absorption. Ground state electrons are provided in the detector by doping the GaAs well layers with Si. This photosensitive MQW structure is sandwiched between  $0.5 \mu\text{m}$  GaAs top and bottom contact layers doped  $n = 5 \times 10^{17} \text{ cm}^{-3}$ , grown on a semi-insulating GaAs substrate by molecular beam epitaxy (MBE). Then a  $0.7 \mu\text{m}$  thick GaAs cap layer on top of a  $300 \text{ \AA}$   $\text{Al}_{0.3}\text{Ga}_{0.7}\text{As}$  stop-etch layer was grown *in situ* on top of the device structure to fabricate the light coupling optical cavity. The epitaxially grown material was processed into  $200 \mu\text{m}$  diameter mesa test structures (area =  $3.14 \times 10^{-4} \text{ cm}^2$ ) using wet chemical etching, and Au/Ge ohmic contacts were evaporated onto the top and bottom contact layers.

The detectors were back illuminated through a  $45^\circ$  polished facet [5] and a responsivity spectrum is shown in Fig. 3. The responsivity of the detector peaks at  $8.5 \mu\text{m}$  and the peak responsivity ( $R_p$ ) of the detector is  $83 \text{ mA/W}$  at bias  $V_B = -1.1 \text{ V}$ . The spectral width and the cutoff wavelength are  $\Delta\lambda/\lambda = 10\%$  and  $\lambda_c = 8.9 \mu\text{m}$  respectively. The measured absolute peak responsivity of the detector is small, up to about  $V_B = -0.5 \text{ V}$ . Beyond that it increases nearly linearly with bias reaching  $R_p = 420 \text{ mA/W}$  at  $V_B = -5 \text{ V}$ . This type of behavior of responsivity versus bias is typical for a bound-to-quasibound QWIP. The peak quantum efficiency was  $1.4\%$  at bias  $V_B = -1.1 \text{ V}$  for a  $45^\circ$  double pass.

The peak detectivity is defined as  $D_p = R_p \sqrt{AB} / I_n$ , where  $R_p$  is the peak responsivity,  $A$  is the area of the detector and  $A = 3.14 \times 10^{-4} \text{ cm}^2$ . The measured peak detectivity at bias  $V_B = -1.1 \text{ V}$  and temperature  $T = 65 \text{ K}$  is  $1 \times 10^{11} \text{ cm}\sqrt{\text{Hz/W}}$ . Figure 4 shows the bias dependence of peak detectivity as a function of temperature. These detectors show BLIP at bias  $V_B = -2 \text{ V}$  and temperature  $T = 72 \text{ K}$  for a  $300 \text{ K}$  background with  $f/2$  optics.

### 3. 640x512 FORMAT FOCAL PLANES

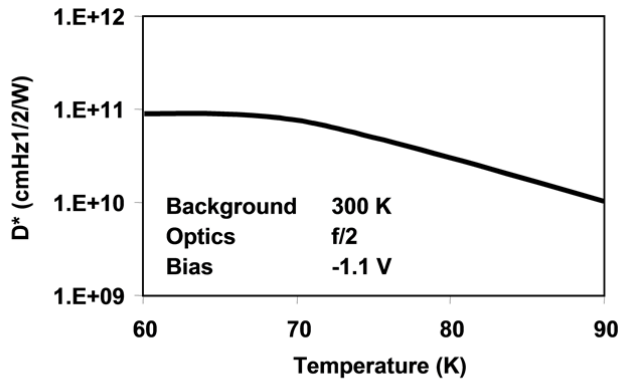


**Fig. 4:** Detectivity as a function of temperatures at bias of 1.1 V.

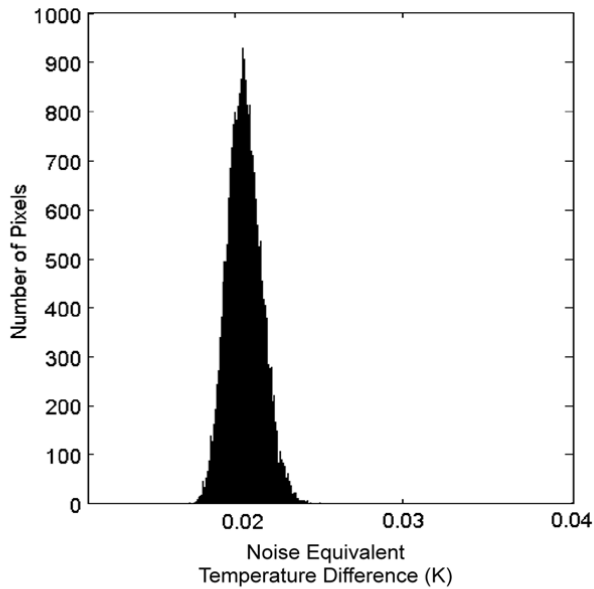


**Fig. 5:** NEDT histogram of the 327,680 pixels of the 640x512 array showing a high uniformity of the FPA.

A 640x512 QWIP FPA hybrid was mounted onto a 330 mW integral Sterling closed-cycle cooler assembly and installed into an Indigo Phoenix™ camera-body, to demonstrate a hand-held LWIR camera (shown in Fig. 6). The Phoenix™ infrared camera system has been developed by Indigo Systems Corporation to meet the needs of the research, industrial and ruggedized OEM communities. The system is comprised of a camera head and a selection of two video processing back ends. The camera head was made of Indigo's standard 640x512 format readout ISC 9803, mated to long-wavelength QWIP detector materials. Two video processing units are the Real Time Imaging Electronics (RTIE) that provide conventional NTSC

After the 2-D grating array was defined by the lithography and reactive ion etching, the photoconductive QWIPs of the 640x512 FPAs were fabricated by dry etching through the photosensitive GaAs/Al<sub>x</sub>Ga<sub>1-x</sub>As multi-quantum well layers into the 0.5 μm thick doped GaAs bottom contact layer. The pitch of the FPA is 25 μm and the actual pixel size is 23x23 μm<sup>2</sup>. The 2-D gratings on top of the detectors were then covered with Au/Ge and Au for Ohmic contact and reflection. Figure 6 shows twelve processed QWIP FPAs on a 3 inch GaAs wafer. Indium bumps were then evaporated on top of the detectors for Si readout circuit (ROC) hybridization. A single QWIP FPA was chosen and hybridized (via indium bump-bonding process) to a 640x512 CMOS multiplexer (ISC 9803) and biased at  $V_B = -1.1$  V. At temperatures below 72 K, the signal to noise ratio of the system is limited by array non-uniformity, multiplexer readout noise, and photo current (photon flux) noise. At temperatures above 72 K, temporal noise due to the QWIP's higher dark current becomes the limitation. This initial array gave excellent images with 99.92% of the pixels working (number of dead pixels  $\approx 250$ ), demonstrating the high yield of GaAs technology. The operability was defined as the percentage of pixels having noise equivalent differential temperature less than 100 mK at 300 K background and in this case operability happens to be equal to the pixel yield. Figure 5 shows the measured NEΔT of the FPA at an operating temperature of  $T = 65$  K, 16 msec integration time, bias  $V_B = -1.1$  V for 300 K background with f/2 optics and the mean value is 20 mK. This agrees reasonably with our estimated value of 10 mK based on test structure data. The net peak quantum efficiency of the FPA was 1.4%

### 4. 640x512 PIXEL HAND-HELD CAMERA AND QUANTITATIVE INFRARED IMAGERY



**Fig. 6:** Picture of the 640x512 hand-held long wavelength QWIP camera (QWIP Phoenix™).

video as well as corrected parallel digital video out at video rates and the Digital Acquisition System (DAS) that provides high-speed (40 MHz) raw digital data acquisition and output with limited real time video for system setup and focusing. The other element of the camera is a 100 mm focal length germanium lens, with a 5.5 degree field of view. It is designed to be transparent in the 7-14  $\mu\text{m}$  wavelength range, to be compatible with the QWIP's 8.5  $\mu\text{m}$  operation. The digital acquisition resolution of the camera is 14-bits, which determines the instantaneous dynamic range of the camera (i.e., 16,384).

The measured mean NE $\Delta$ T of the QWIP camera is 20 mK (the higher NEDT is due to the 65% transmission through the lens assembly) at an operating temperature of  $T = 65\text{ K}$  and bias  $V_B = -1.1\text{ V}$ , for a 300 K background with germanium f/2 optics. The uncorrected photocurrent non-uniformity (which includes a 1% non-uniformity of the ROIC and a 1.4% non-uniformity due to the cold-stop in front of the FPA not yielding the same field of view to all the pixels) of the 327,680 pixels of the 640x512 FPA is about 5% (= sigma/mean). The non-uniformity after two-point (17° and 27° Celsius) correction improves to an impressive 0.02%. After correction, measurements of the residual non-uniformity were made at temperatures ranging from 12 Celsius (the cold temperature limit of the blackbody) up to 42 degrees Celsius. The non-uniformity at each temperature was found by averaging 16 frames, calculating the standard deviation of the pixel-to-pixel variation of the 16 frames average and then dividing by the mean output, producing non-uniformity that may be reported as a percentage. For camera systems that have NE $\Delta$ T of about 20 mK, the corrected image must have less than 0.1% non-uniformity in order to be TV quality. Figure 7 shows the residual non-uniformity of the camera after two-point correction as a function of scene temperature. Also it is clearly evident from Fig. 7 that the camera's performance is outstanding in this scene temperature range, and its residual non-uniformity did not exceed 0.03% within the entire scene temperature range of 12 – 42 Celsius.

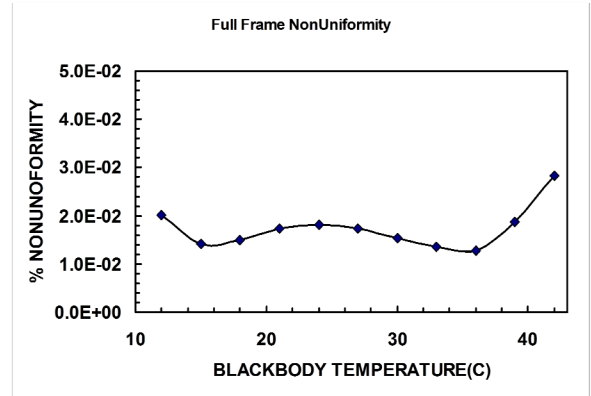


**Fig. 7.** Residual non-uniformity after two-point correction as a function of scene temperature. This corrected non-uniformity range is comparable to 3-5  $\mu\text{m}$  infrared cameras.

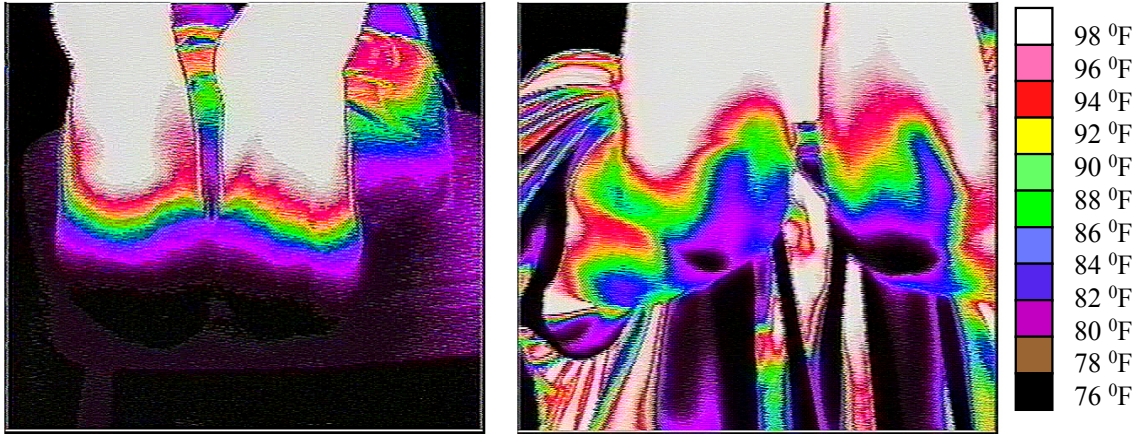


**Fig. 8.** This figure shows the temperature variation of the toes and elbows of a leprosy patient.

Video images were taken at a frame rate of 30 Hz at temperatures as high as  $T = 65\text{ K}$ , using a ROIC capacitor having a charge capacity of  $11 \times 10^6$  electrons (the maximum number of photoelectrons and dark electrons that can be counted in the time taken to read each detector pixel). Figure 8 shows one frame of a video image taken with a 9  $\mu\text{m}$  cutoff 640x512 pixel QWIP Phoenix™ camera. The temperature was calculated assuming 0.8 emissivity using the following equation,

$$I_p = R_p G \int_{\lambda_L}^{\lambda_H} d\lambda [\varepsilon(\lambda) M(\lambda, T_T)] \tilde{R}(\lambda)$$

where,  $G$ ,  $R(\lambda)$ ,  $E(\lambda)$ ,  $\lambda_L$ ,  $\lambda_H$ ,  $M(\lambda, T_T)$ , and  $R_P$  are the optical gain, normalized responsivity versus wavelength function, emissivity as a function of wavelength, lower and upper limit of the detector wavelength response, spectral exitance of the source at temperature, and peak responsivity of the detector respectively.

## 5. DUAL-BAND INFRARED IMAGERY

The spectral response of QWIPs are inherently narrow-band and the typical full-width at half-maximum (FWHM) is about 10% of the peak wavelength. This makes it suitable for fabrication of negligible optical cross-talk dual-band detector arrays. This shortfall in single band detector measurement due to unknown emissivity can be overcome by taking the ratio of the signals measured at two different wavelengths using a dual-band detector. If we assume negligible variation of emissivity in thermal infrared wavelength range essentially produces a dual-band signal ratio, which is a singular function of the source temperature.

$$\frac{\phi_{\text{det } 1}}{\phi_{\text{det } 2}} = \frac{\int_{\Delta\lambda 1} M(\lambda, T) R_1(\lambda) S_1(\lambda) d\lambda}{\int_{\Delta\lambda 2} M(\lambda, T) R_2(\lambda) S_2(\lambda) d\lambda}$$

Here  $M(\lambda, T)$  is the spectral exitance of the source at temperature,  $T$ ,  $R(\lambda)$  is the spectral responsivity of the detector, and  $S(\lambda)$  is the optical transfer function of the measurement system. As shown in above equation, the flux received by the detector ( $\phi_{\text{det}}$ ) is directly proportional to the emissivity of the source,  $\epsilon$ :  $0 < \epsilon \leq 1$ . Figure 9 shows estimated signal ratio of a  $4.4\mu\text{m} - 5.1\mu\text{m}$  MWIR and a  $8\mu\text{m} - 9\mu\text{m}$  LWIR dual band detector as a function of source temperature for different emissivities. The uncorrected signal ratio plotted in Figure 9(a) still shows range of source temperatures for a given signal ratio. The variation in signal ratio with different emissivities arises due to background (optics/windows & dark

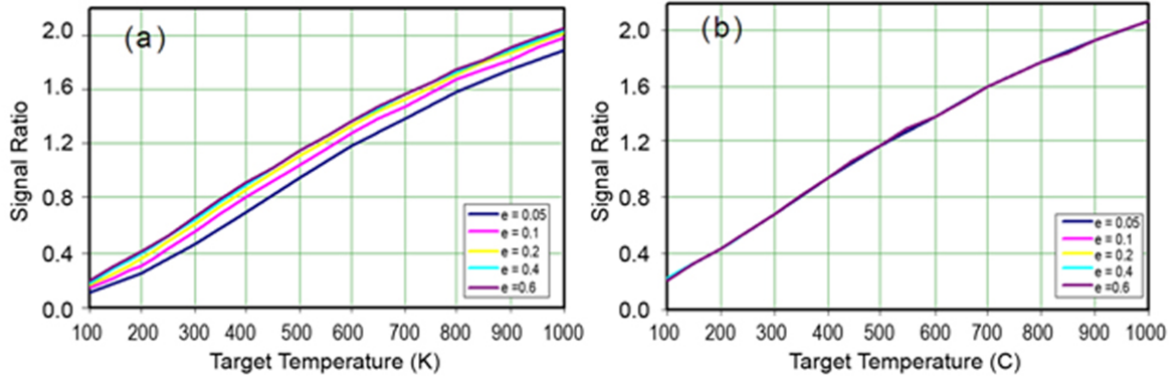


**Fig. 9.** (a) The ratio of the dual-band signals versus source temperature with different source emissivities. The spreading of curves in uncorrected signal ratio is due to the background signals of the system that can be corrected using a cold-shutter. (b) Corrected signal ratio curves illustrate accurate measurement of source temperature regardless of the emissivity. It's worth noticing that all curves overlap as expected after the background correction.

currents) of the system signal that can be subtracted to obtain the corrected signal ratio. Figure 9(b) clearly shows the overlap of signal ratio vs. source temperature curves, illustrating the accurate temperature reading of the source regardless of the emissivity. In practice, background subtraction is easily implemented by using a cold shutter in the camera system.

## 6. PIXEL CO-REGISTERED SIMULTANEOUSLY READABLE DUAL-BAND QWIP DEVICE

A coupled-quantum well structure was used in this device to broaden the responsivity spectrum. In the MWIR device, each period of the MQW structure contains a 300 Å thick un-doped barrier of  $\text{Al}_{0.25}\text{Ga}_{0.75}\text{As}$ , and a double quantum well region. The double QW region contains two identical quantum wells separated by a 45 Å of  $\text{Al}_{0.25}\text{Ga}_{0.75}\text{As}$  un-doped barrier. Each of the two quantum wells consists of 3 Å AlAs, 5 Å GaAs, 32 Å  $\text{In}_{0.3}\text{Ga}_{0.7}\text{As}$ , 5 Å GaAs, and 3 Å AlAs; the quantum well is doped  $n = 4 \times 10^{18} \text{ cm}^{-3}$ . This period was repeated 13 times. In the LWIR device, each period of the MQW structure contains a 580 Å thick un-doped of  $\text{Al}_{0.25}\text{Ga}_{0.75}\text{As}$  barrier, and a triple quantum well region. The triple QW region contains three identical 50 Å GaAs quantum wells (doped to  $n = 5 \times 10^{17} \text{ cm}^{-3}$ ) separated by 50 Å of



$\text{Al}_{0.25}\text{Ga}_{0.75}\text{As}$  un-doped barriers. This period was repeated 16 times. These two photosensitive MQW structures are sandwiched between GaAs top and bottom contact layers doped  $n = 1 \times 10^{18} \text{ cm}^{-3}$ , grown on a semi-insulating GaAs substrate by molecular beam epitaxy (MBE). Top contact was a  $0.7 \text{ }\mu\text{m}$  thick GaAs cap layer on top of a  $350 \text{ }\text{\AA}$   $\text{Al}_{0.25}\text{Ga}_{0.75}\text{As}$  stop-etch layer grown *in situ* on top of the dual-band device structure to fabricate the light coupling optical cavity [9-12]. The bottom contact layer was a  $2 \text{ }\mu\text{m}$  thick GaAs layer. A  $0.4 \text{ }\mu\text{m}$  thick un-doped AlGaAs layer was embedded between the top contact of the LWIR and bottom contact of the MWIR MQW regions. As shown in Fig. 10, the MWIR device uses a bound-to-continuum design to help further broaden the spectrum; a single monolayer of AlAs on each side of quantum well is used to help increase the oscillator strength. The LWIR device uses a standard bound-to-quasibound design, where the upper levels involved in the infrared optical transition is in approximate resonance with the conduction band edge of the barrier. Note that the same AlGaAs barrier composition is used throughout the structures

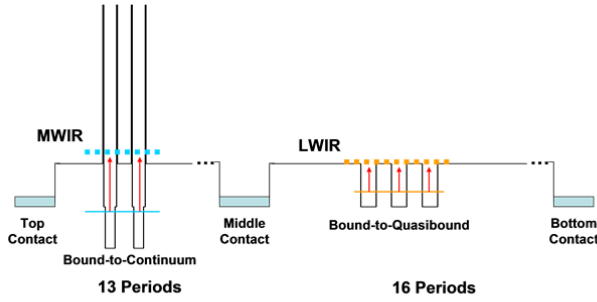


**Fig 10.** Energy band diagram of the dual-band QWIP structure.

We modeled the device structures using a two-band model that includes band non-parabolicity effects [9], with material parameters taken from Reference [10]. For the LWIR structure, the calculated energy levels of the ground states in the unbiased triple-well are found to be at 147 meV, 151 meV, and 155 meV below the AlGaAs barrier, while the upper states are in approximate resonance with the top of the barrier. For the MWIR structure, the energy levels of the ground states in the unbiased double-well are found to be at 276 meV and 277 meV below the AlGaAs

barrier, while the upper states are slight above the top of the barrier. The modeling results are found to be in good agreement with experimental results. It is worth noting that the photo-sensitive MQW region of each QWIP device is transparent at other wavelengths which is an important advantage over conventional interband detectors. This spectral transparency makes QWIP an attractive detector material for pixel co-located dual-band FPAs with minimal spectral cross-talk.

The MBE grown material was tested for absorption efficiency using a Fourier Transform Infrared (FTIR) spectrometer. The experimentally measured peak absorption (or internal) quantum efficiency ( $\eta_a$ ) of this material at room temperature was 19%. The epitaxially grown material was processed into  $200 \text{ }\mu\text{m}$  diameter mesa test structures (area =  $3.14 \times 10^{-4} \text{ cm}^2$ ) using wet chemical etching, and Au/Ge ohmic contacts were evaporated onto the top and bottom contact layers. The detectors were back illuminated through a  $45^\circ$  polished facet and a responsivity spectrum is shown in Fig. 11. The responsivity of the detector peaks at  $4.6 \text{ }\mu\text{m}$  and the peak responsivity ( $R_p$ ) of the detector is  $170 \text{ mA/W}$  at bias  $V_B = -1 \text{ V}$ . The spectral width and the cutoff wavelength are  $\Delta\lambda/\lambda = 15\%$  and  $\lambda_c = 5.1 \text{ }\mu\text{m}$  respectively. The peak detectivity is the

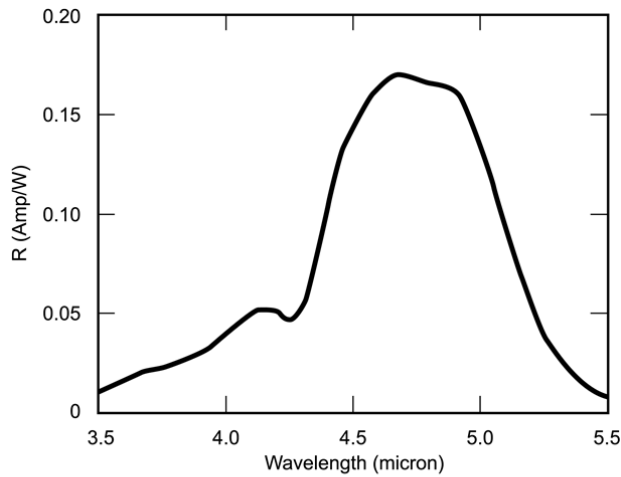


**Fig 11.** Responsivity spectrum of a bound-to-quasi-bound MWIR QWIP test structure at temperature  $T = 77 \text{ K}$ . The spectral response peak is at  $4.6 \text{ }\mu\text{m}$  and the long wavelength cutoff is at  $5.1 \text{ }\mu\text{m}$ .

peak signal-to-noise ratio normalized to unit area and bandwidth and given by  $D_p^* = R_p \sqrt{A} / i_n$ , where  $R_p$  is the peak responsivity (defined earlier), and  $A$  is the area of the detector  $A = 3.14 \times 10^{-4} \text{ cm}^2$ . The noise current  $i_n$  is given by the shot noise of the total current  $I$  (i.e., dark current + photo current) and given by  $i_n = (4eI B)^{1/2}$ . The measured peak detectivity at bias  $V_B = -1 \text{ V}$  and temperature  $T = 90 \text{ K}$  is  $4 \times 10^{11} \text{ cm}^2/\text{Hz/W}$ . These detectors show BLIP at a bias  $V_B = -1 \text{ V}$  and temperature  $T = 90 \text{ K}$  for  $300 \text{ K}$  background with  $f/2.5$  optics.

The experimentally measured LWIR responsivity spectrum is shown in Fig. 12. The responsivity of the detector peaks at  $8.4 \text{ }\mu\text{m}$  and the peak responsivity ( $R_p$ ) of the detector is  $130 \text{ mA/W}$  at bias  $V_B = -1 \text{ V}$ . The spectral width and the cutoff wavelength are  $\Delta\lambda/\lambda = 10\%$  and  $\lambda_c = 8.8 \text{ }\mu\text{m}$ , respectively. The photoconductive gain  $g$  was experimentally determined as described in the previous section. The peak detectivity of the LWIR detector was calculated using experimentally measured

noise current  $i_n$ . The calculated peak detectivity at bias  $V_B = -1$  V and temperature  $T = 70$  K is  $1 \times 10^{11}$  cm  $\sqrt{\text{Hz}}/\text{W}$ . These detectors show BLIP at bias  $V_B = -1$  V and temperature  $T = 72$  K for a 300 K background with f/2.5 optics.

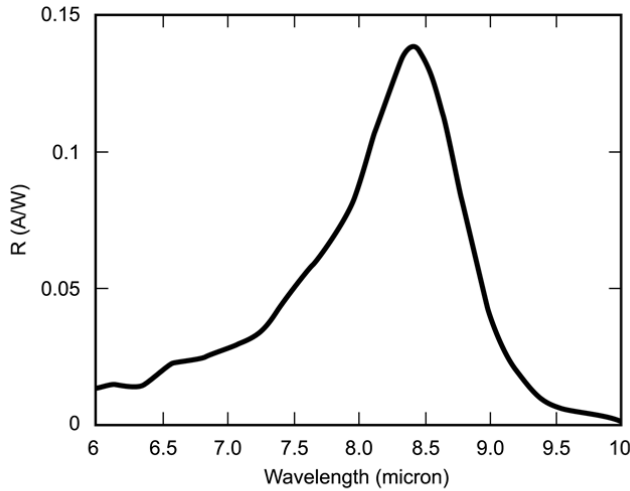


**Fig 12.** Responsivity spectrum of a bound-to-quasibound LWIR QWIP test structure at temperature  $T = 77$  K. The spectral response peak is at  $8.4 \mu\text{m}$  and the long wavelength cutoff is at  $8.8 \mu\text{m}$ .

metal was removed using a metal lift-off process. The pitch of the detector array is  $30 \mu\text{m}$  and the actual MWIR and LWIR pixel sizes are  $28 \times 28 \mu\text{m}^2$ . Five detector arrays were processed on a four-inch GaAs wafer. Indium bumps were then evaporated on top of the detectors for hybridization with ROICs. Several dual-band detector arrays were chosen and hybridized (via an indium bump-bonding process) to grade-A 1024x1024 pixel dual-band silicon ROICs. Figure 13 shows a megapixel dual-band QWIP FPA mounted on a 124 pin LCC.

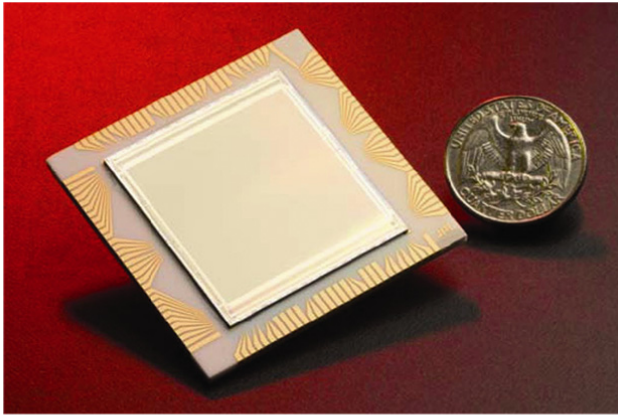


**Fig. 13.** Picture a 1024x1024 pixel dual-band QWIP FPA mounted on a 124-pin lead less chip carrier.

## 7. 1024X1024 PIXEL DUAL-BAND QWIP FOCAL PLANE ARRAY

After the 2-D grating array was defined by stepper based photolithography and dry etching, the MWIR detector pixels of the 1024x1024 pixel detector arrays, and the via-holes to access the detector-common, were fabricated by dry etching through the photosensitive GaAs/In<sub>y</sub>Ga<sub>1-y</sub>As/Al<sub>x</sub>Ga<sub>1-x</sub>As MQW layers into the  $0.5 \mu\text{m}$  thick doped GaAs intermediate contact layer. Then LWIR pixels and via-holes for MWIR pixels to access the array detector-common were fabricated. A thick insulation layer was deposited and contact windows were opened at the bottom of each via-hole and on the top surface. Ohmic contact metal was evaporated and unwanted

A MWIR:LWIR pixel co-registered simultaneously readable dual-band QWIP FPA has been mounted onto the cold finger of a pour fill dewar, cooled by liquid nitrogen, and the two bands (i.e., MWIR and LWIR) were independently biased. Some imagery was performed at a temperature of 68 K. An image taken with the first megapixel simultaneous pixel co-registered MWIR:LWIR dual-band QWIP camera is shown in Fig.14. The flame in the MWIR image (left) looks broader due to the detection of heated CO<sub>2</sub> (from a cigarette lighter) re-emission in a 4.1–4.3-micron band, whereas the heated CO<sub>2</sub> gas does not have any emission line in the LWIR (8–9 microns) band. Thus, the LWIR image shows only thermal signatures of the flame. This initial array gave good images with 99% of the MWIR and 97.5% of the

LWIR pixels working in the center  $512 \times 512$  pixels region, which is excellent compared to the difficulty in the fabrication process of this pixel co-registered simultaneously readable dual-band QWIP FPA. The digital acquisition resolution of the imaging system was 14-bits, which determines the instantaneous dynamic range of the camera (i.e., 16,384). However, the dynamic range of QWIP is 85 Decibels. Video images were taken at a frame rate of 30 Hz at temperatures as high as  $T = 68$  K. The total ROIC well depth is  $17 \times 10^6$  electrons with LWIR to MWIR well depth ratio of 4:1.

NE $\Delta$ T provides the thermal sensitivity of an infrared imaging system and it is a very useful diagnostic tool to evaluate the full operational performance available. It is defined as the minimum temperature difference required at the target to produce signal-to-noise-ratio of one. We have used the following equation to calculate the noise equivalent temperature difference NE $\Delta$ T of the FPA.

$$NE\Delta T = \frac{\sqrt{AB}}{D_B^* (dP_B / dT) \sin^2(\theta / 2)}$$

Where  $D_B^*$  is the blackbody detectivity,  $dP_B/dT$  is the derivative of the integrated blackbody power with respect to temperature, and  $\theta$  is the field of view angle [i.e.,

$\sin^2(\theta/2) = (4f^2 + 1)^{-1}$ , where  $f$  is the  $f$  number of the optical system]. The estimated NE $\Delta$ T based on single pixel data of MWIR and LWIR detectors at 68 K are 22 and 24 mK, respectively.

Sequence of consecutive frames is collected for equivalent noise determination as well as other optical properties of FPA. The photo response matrices of FPA is derived at the low and high blackbody temperatures (i.e., 295 K and 305 K), and temporal noise matrix of FPA is estimated at the mid-point temperature by taking 64 frames of data. The temporal NE $\Delta$ T of pixels are numerically evaluated from the relations,  $NE\Delta T = \sigma_{\text{Temporal}} \Delta T / [\text{Mean}(T_H) - \text{Mean}(T_L)]$ . The mean signal  $\text{Mean}(T_L)$  and  $\text{Mean}(T_H)$  are evaluated at blackbody temperatures of  $T_L = 295$  K and  $T_H = 305$  K. The temporal noise is measured at 300K using 64 frames, and  $\Delta T \sim 10$  K. The measured mean NE $\Delta$ T was estimated at 27 and 40 mK for MWIR and LWIR bands respectively at a flat plate blackbody temperature of 300K with  $f/2$  cold stop.

The experimentally measured NE $\Delta$ T histograms distributions at blackbody temperature of 300 K with  $f/2$  cold stop are shown in the Fig. 15 (a) and (b). The experimentally measured MWIR NE $\Delta$ T value closely agrees with the estimated NE $\Delta$ T value based on the results of a single element test detector data. However, the measured LWIR NE $\Delta$ T value is higher than the estimated NE $\Delta$ T value based on the single pixel data. This is due to the fact that we could not completely independently optimize the operating bias of LWIR band due to a ROIC pixel short circuit occurred at the MWIR band.



**Fig. 14.** An image taken with the first megapixel simultaneous pixel co-registered MWIR:LWIR dual-band QWIP camera. The flame in the MWIR image (left) looks broader due to the detection of heated CO<sub>2</sub> (from cigarette lighter) re-emission in 4.1–4.3-micron band, whereas the heated CO<sub>2</sub> gas does not have any emission line in the LWIR (8–9 microns) band. Thus, the LWIR image shows only thermal signatures of the flame.

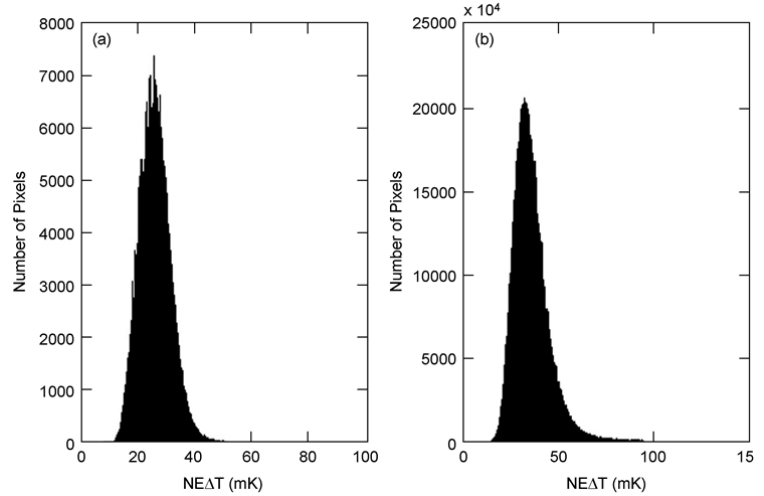


**Fig. 15.** NE $\Delta$ T histogram of the 1024x1024 format simultaneously readable pixel co-registered dual-band QWIP FPA. Each spectral band of the FPA consisted of co-registered megapixel. The experimentally measured NE $\Delta$ T of MWIR and LWIR detectors at 68 K are 27 and 40 mK, respectively.



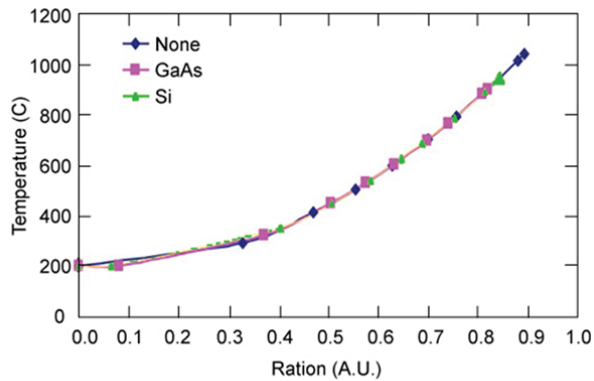


**Fig. 16.** MWIR:LWIR signal ratio as a function of scene temperature.

We have calibrated this dual-band MWIR:LWIR sensor against a standard calibrated blackbody at various temperatures from 100-1000C. Figure 16 shows the experimentally measured MWIR:LWIR dual-band signal ratio as a function of blackbody scene temperature. Using this curve we could derive the scene (or target) temperature without knowing the emissivity of the target assuming that emissivity is not changing as a function of wavelength between the MWIR and LWIR spectral regions. Figure 17 shows the MWIR and LWIR images of three different plates approximately heated to above 300C. The absolute temperature of these targets were measured by a precision pre-calibrated thermocouple attached to each plate. The LWIR and MWIR signal counts are 3508 and 1602 ADUs respectively for the white painted aluminum plate. This ratio of 0.46 yields

approximately 400C as the target temperature of the white painted aluminum plate. The thermocouple reading of the white painted aluminum plate was 344C. The remote temperature measurement error was 16.27% and most of that inaccuracy is attributed the fact that emissivity is a constant value between these two spectral regions.

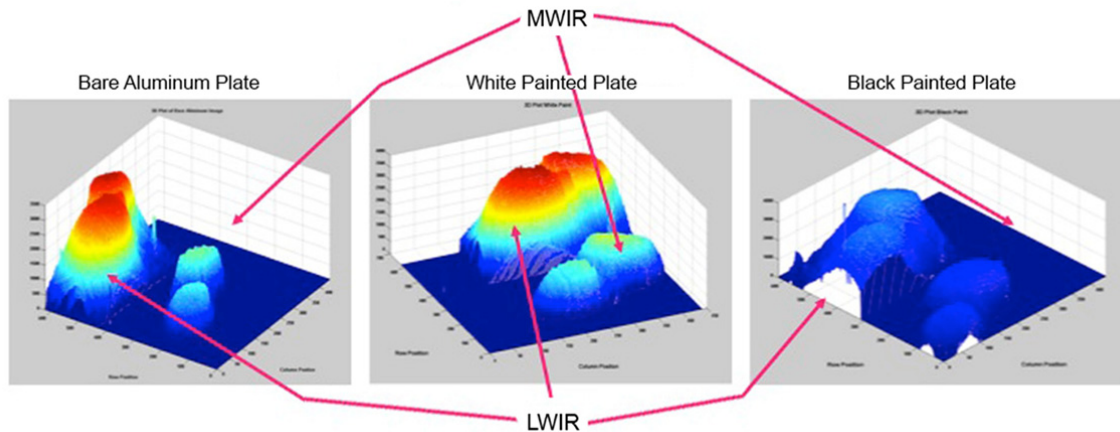


**Fig. 17.** 3D intensity verses area dual-band infrared (MWIR and LWIR) imagery of target plates, (a) bare aluminum plate at 300C, (b) white painted aluminum plate at 344C, and (c) black painted aluminum plate at 344C.

## 9. NEW DIRECTIONS IN SURFACE TEMPERATURE MEASUREMENTS USING MULTIBAND RADIOMETRY

We are currently developing a four-color spatially separated 2x2 super pixel IR FPA, since surface emissivities are a function of wavelength and dual-band is not sufficient to accurately remote sense target surface temperature. See figure 18 for a picture of a 4-color QWIP IR FPA is being developed for the remote target surface temperature measurement applications. When attempting to determine the target surface temperature of an object based on radiometric measurements in multiple infrared wavebands, the number of unknowns (the temperature plus each waveband emissivity) is greater than the number of IR waveband measurements.

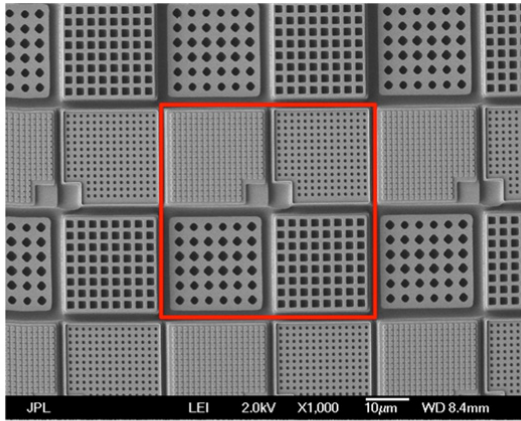


**Fig. 18.** Scanning Electron Micrograph (SEM) of a four-band QWIP detector array. The red square in the middle shows the 2x2 super pixel.

Thus, it is essential to have some additional information about the emissivity, so that the number of unknowns is reduced, and an accurate value for temperature can be obtained. One method that has been considered is to represent the spectral emissivity as a simple analytical function, which contains fewer parameters than the number of wavebands. This approach was investigated using multiple wavebands. These calculations show that remote accurate temperature sensing is possible if the emissivity form used in the solution is capable of representing the true emissivity. But, inaccurate temperature values will be produced if the emissivity form used in the calculation is not accurately representing the true emissivity of the target surface. We feel that it is impossible to accurately remote sense the target surface temperature by assuming a simple analytical form for the spectral shape of the true emissivity of the target surface if it is unknown. In conclusion, some a priori knowledge of the target surface emissivity is required (i.e.,

to reduce the number of unknowns) for accurate remote sensing of target surface temperature.

## 10. ACKNOWLEDGMENT

The authors thank R. Liang, M. Herman and E. Kolawa of JPL and M. Tidrow, of the U.S. Army Night Vision Electronics Sensor Directorate. The research described in this paper was carried out at the Jet Propulsion Laboratory, California Institute of Technology and government sponsorship acknowledged. Copyright 2012 California Institute of Technology.

## REFERENCES

- [1] S. D. Gunapala, S. V. Bandara, S. B. Rafol, and D. Z. Ting, "Quantum Well Infrared Photodetectors," *Semiconductors and Semimetals*, Vol. 84, 59-151, Academic Press, 2011.
- [2] S. D. Gunapala, J. K. Liu, J. S. Park, T. L. Lin, and M. Sundaram "Infrared Radiation Detecting Device", US Patent No. 6,211,529.
- [3] Sarath D. Gunapala, John K. Liu, Jin S. Park, Mani Sundaram, Craig A. Shott, Ted Hoelter, True-Lon Lin, S. T. Massie, Paul D. Maker, Richard E. Muller, and Gabby Sarusi "9  $\mu\text{m}$  Cutoff 256x256 GaAs/AlxGa1-xAs Quantum Well Infrared Photodetector Hand-Held Camera", *IEEE Trans. Electron Devices*, 44, pp. 51-57, 1997.
- [4] W. Cabanski, R. Breiter, R. Koch, K. H. Mauk, W. Rode, J. Ziegler, H. Schneider, M. Walther, and R. Oelmaier, *SPIE Vol. 4369*, pp. 547-558 (2001).
- [5] S. D. Gunapala and S. V. Bandara, "Quantum Well Infrared Photodetector (QWIP) Focal Plane Arrays," *Semiconductors and Semimetals*, Vol. 62, 197-282, Academic Press, 1999.
- [6] S. D. Gunapala, S. V. Bandara, A. Singh, J. K. Liu, S. B. Rafol, E. M. Luong, J. M. Mumolo, N. Q. Tran, J. D. Vincent, C. A. Shott, J. Long, and P. D. LeVan, "640x486 Long-wavelength Two-color GaAs/AlGaAs Quantum Well Infrared Photodetector (QWIP) Focal Plane Array Camera" *IEEE Trans. Electron Devices*, 47, pp. 963-971, 2000.
- [7] S. D. Gunapala, S. V. Bandara, J. K. Liu, E. M. Luong, S. B. Rafol, J. M. Mumolo, D. Z. Ting, J. J. Bock, M. E. Ressler, M. W. Werner, P. D. LeVan, R. Chehayeb, C. A. Kukkonen, M. Levy, P. LeVan, and M. A. Fauci, "Infrared Physics & Technology, Vol. 42, pp. 267-282, (2001).
- [8] E. L. Dereniak and G. D. Boreman, "Infrared Detectors and Systems" ISBN:0-471-12209-2, Wiley-Interscience, John Wiley & Sons, Inc., New York, 1996.
- [9] D. Z.-Y. Ting, E. T. Yu, D. A. Collins, D. H. Chow, and T. C. McGill, "Modeling of Novel Heterojunction Structures," *J. Vac. Sci. Technol. B* 8, 810-816 (1990).
- [10] I. Vurgaftman, J. R. Meyer, and L. R. Ram-Mohan, "Band parameters for III-V compound semiconductors and their alloys," *J. Appl. Phys.* 89, 5815-5875 (2001).